

PAPER • OPEN ACCESS

Improving a high-power laser-based relativistic electron source: the role of laser pulse contrast and gas jet density profile

To cite this article: A Grigoriadis *et al* 2022 *Plasma Phys. Control. Fusion* **64** 044007

View the [article online](#) for updates and enhancements.

You may also like

- [Numerical and experimental study of the behaviour of a single-axis fluidic thermal gyroscope](#)
Guillaume Kock, Philippe Combette, Marwan Tedjini *et al.*
- [Brilliance improvement of laser-produced soft x-ray plasma by a barrel shock](#)
Tobias Mey, Martin Rein, Peter Großmann *et al.*
- [The characterization of a high-density gas jet](#)
A Behjat, G J Tallents and D Neely

Improving a high-power laser-based relativistic electron source: the role of laser pulse contrast and gas jet density profile

A Grigoriadis^{1,2}, G Andrianaki^{2,3}, I Fitis^{2,4} , V Dimitriou^{2,5} , E I Clark², N A Papadogiannis^{2,5} , E P Benis¹  and M Tatarakis^{2,4,*} 

¹ Department of Physics, University of Ioannina, 45110 Ioannina, Greece

² Institute of Plasma Physics and Lasers, Hellenic Mediterranean University Research Centre, 74100 Rethymno, Greece

³ School of Production Engineering and Management, Technical University of Crete, 73100 Chania, Greece

⁴ Department of Electronic Engineering, Hellenic Mediterranean University, 73133 Chania, Greece

⁵ Department of Music Technology and Acoustics, Hellenic Mediterranean University, 74133 Rethymno, Greece

E-mail: mictat@hmu.gr

Received 31 October 2021, revised 6 January 2022

Accepted for publication 13 January 2022

Published 18 February 2022



Abstract

A relativistic electron source based on high power laser interaction with gas jet targets has been developed at the Institute of Plasma Physics and Lasers of the Hellenic Mediterranean University. Initial measurements were conducted using the ‘Zeus’ 45 TW laser with peak intensities in the range of 10^{18} – 10^{19} W cm⁻² interacting with a He pulsed gas jet having a 0.8 mm diameter nozzle. A significant improvement of the electron signal was measured after using an absorber to improve the laser pulse contrast from 10^{-10} to 10^{-11} . A high stability quasi-mono-energetic electron beam of about 50 MeV was achieved and measured using a magnetic spectrometer for pulsed gas jet backing pressure of 12 bar. Supplementary studies using a 3 mm diameter nozzle for backing pressures in the range of 35–40 bar showed electron beam production with energies spread in the range from 50 to 150 MeV. The pulsed jet density profile was determined using interferometric techniques. Particle-in-cell simulations, at the above experimentally determined conditions, support our experimental findings.

Keywords: laser wakefield acceleration (LWFA), laser plasma interaction, electron beams

(Some figures may appear in color only in the online journal)

1. Introduction

Laser wakefield acceleration (LWFA) [1] is a hot topic due to the wide variety of possible applications including, among others, the production of betatron-type radiation, thus providing

a coherent x-ray source which is one of the most promising backlighter diagnostics in studying high energy density physics and inertial confinement fusion [2]. Certainly, LWFA has been one of the pioneering methods for accelerating electrons to energies ranging from tens of MeV [3–5] up to GeV [6–12]. Modern laser systems, reaching powers of TW [13] or even PW [14, 15] are nowadays becoming available in laboratories worldwide, thus offering the possibility for the development

* Author to whom any correspondence should be addressed.



of secondary relativistic electron sources based on LWFA. The optimization of the electron beam characteristics of such sources, i.e. the beam current, the energy spectrum, the maximum attainable energy, the monochromaticity and the angular divergence, is of vital importance. Many publications have been reported in the literature with focus on the improvement of the electron acceleration conditions in terms of gas target selection and jet geometry [16–21], injection mechanism control [22–24] and laser pulse characteristics [25].

In this work we present experimental findings for the optimization of our LWFA electron source at the Institute of Plasma Physics and Lasers (IPPL) of the Hellenic Mediterranean University. After the development of the source, the effort on optimizing its operation was primarily focused on the laser pulse contrast and the gas density profile. In terms of the laser pulse contrast, previous studies have shown that the electron beam pointing stability is improved by increasing the laser pulse contrast [26]. However, these studies were performed using different laser contrast levels in different experimental configurations. Later studies using different laser contrast at the same experimental configuration showed significant changes on electron beam profiles, used for probing magnetic fields during high-intensity laser–solid interactions [27]. Here, we present results taken at two different laser contrast levels acquired at the same experimental conditions, clearly showing that the higher laser contrast level results in improved electron beam stability conditions. In terms of the target density profile, we performed studies using two different gas jet geometries, corresponding to different electron acceleration lengths, thus showing the dependence of the characteristics of the generated electron spectrum on the gas density profile. These experimental findings are supported by particle in cell (PIC) simulations, designed for the experimentally determined conditions. Our relativistic electron beam source has already been applied in testing space electronic devices as well as irradiating polymeric gel dosimeters [28] and biological samples. In addition, studies of this source including the simultaneous detection of the generated betatron-type x-ray radiation and the relativistic electrons, have been recently reported [29, 30].

2. The experimental setup

The experiments were performed using the 45 TW fs laser system ‘Zeus’ of the IPPL [13]. The laser system, manufactured by Amplitude Technologies, delivers pulses with a maximum energy of 1.3 J, central wavelength at 800 nm and duration of 23 fs, at a repetition rate up to 10 Hz. The experimental setup developed to produce secondary relativistic electron beams is illustrated in figure 1. The main laser beam, delivered by the laser system in vacuum at the interaction chamber, was focused by a 1 m focal length parabolic mirror ($f/18$) resulting in a focal spot with a diameter of $30\ \mu\text{m}$ at full width at half maximum (FWHM). Thus, the peak intensity at the interaction region was of the order of 10^{18} – $10^{19}\ \text{W cm}^{-2}$. A secondary 25 fs, 10 mJ laser beam, delivered by the first stage of amplification, was used for monitoring the interaction region via shadowgraphy, when necessary.

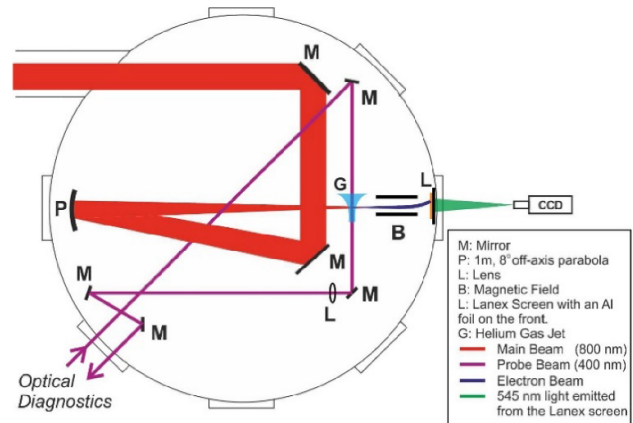


Figure 1. The experimental setup of the relativistic electron source.

The target was a pulsed helium gas jet operated using an electromagnetic valve (Parker). Two different gas profile geometries were examined by replacing the nozzles at the exit opening of the electromagnetic valve. The first nozzle was cylindrical with a 0.8 mm diameter while the second was conical having a 3 mm diameter exit. The backing pressure for the optimum acceleration conditions was experimentally determined to be at 12 bar for the cylindrical nozzle and at 35 bar for the conical nozzle. The relativistic electrons signal was recorded in two geometries: (a) along the laser beam propagation axis on a scintillating screen (Lanex Regular), after properly blocking the laser light with a $13\ \mu\text{m}$ thick Al foil placed in front of the screen; (b) using a magnetic spectrometer consisting of two permanent magnets ($11\ \text{cm} \times 9\ \text{cm}$) placed in parallel at a separation distance of 1 cm. The resulting nearly homogeneous magnetic field was measured with a Hall probe to be 0.4 T. The deflected electron beam was then guided onto a scintillating screen (Lanex Regular) and the emitted light from the rear side of the screen was imaged by a lens onto a charge-coupled device (CCD) camera. The front size of the scintillating screen was also covered with a $13\ \mu\text{m}$ thick Al foil to shield it from laser light. The electron energy spectra were extracted from the recorded deflection of the electrons on the scintillating screen based on the tracking of relativistic electrons through the magnetic field geometry. By calibrating the screen imaging system using a laser light source, we were able to estimate the number of accelerated electrons for each laser shot. Specifically, a continuous wave (CW) laser beam was used as a light source having a wavelength of 541 nm which is essentially the same with the one emitted from the Lanex screen (545 nm). By selecting a 20 ms temporal operation window in the CCD camera software, 5.44×10^{14} photons were recorded. The Lanex screen electron-to-photon conversion efficiency was estimated based on reports about absolute calibration of similar electron spectrometers [31, 32]. Then, by considering the CCD camera gain and quantum efficiency, the correction for the solid angle of detection and the transparency of the camera imaging lens, we estimated a typical conversion efficiency of 6.6×10^{-5} pC/pixel in an 8 bit grayscale for the total imaging system, i.e. Lanex screen, imaging lens and CCD camera.

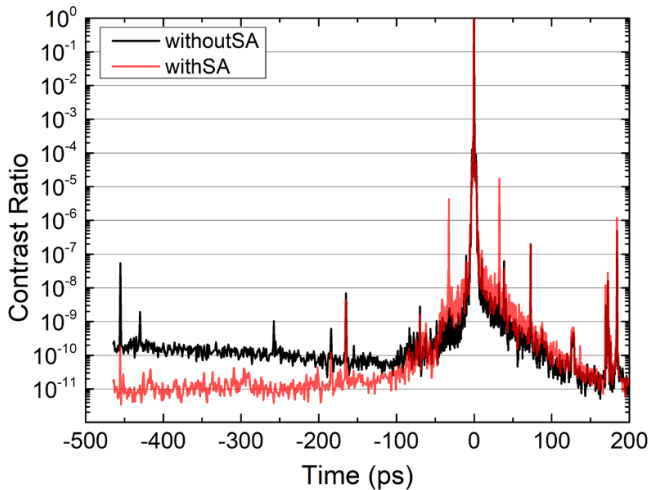


Figure 2. Laser pulse 3rd order autocorrelation with and without using the saturable absorber.

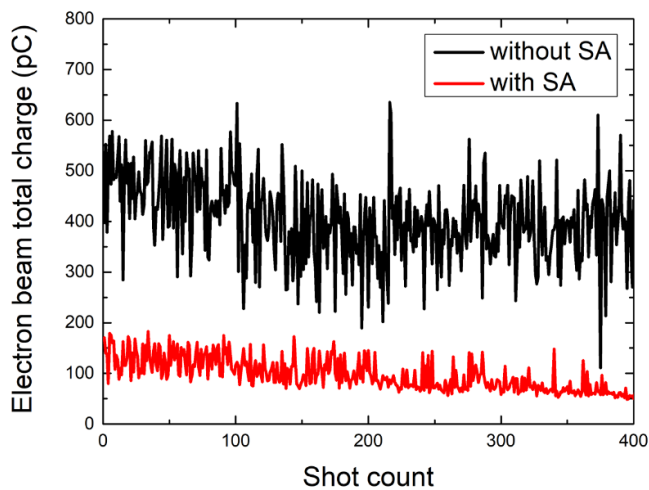


Figure 3. Shot-to-shot total electron beam charge for a total of 400 consecutive shots with and without using the saturable absorber.

3. The laser pulse contrast

The effect of the laser pulse contrast on the generation of the relativistic electron beam was investigated by reducing the level of the laser pulse amplified spontaneous emission (ASE) pedestal. The laser system was initially delivered with a contrast ratio between 10^{-9} and 10^{-10} . A contrast improvement by an order of magnitude was achieved by installing a saturable absorber (Schott RG850) inside the laser beam path, after the temporal stretching of the pulse. In figure 2 we present the laser pulse 3rd order autocorrelation which clearly illustrates that the ASE pedestal intensity is reduced by more than one order of magnitude for $t < 100$ ps before the laser pulse peak, when the absorber is in use. This increase of the contrast had a straightforward effect on the stability of the relativistic electron beam. In figure 3 we present a 400 consecutive shot-to-shot measurements of the total charge of the electron beam deposited on the scintillating screen for both contrast cases. In this case, the electrons were detected without the use of the

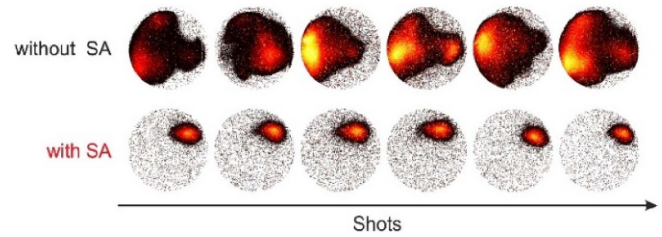


Figure 4. Shot-to-shot electron beam profiles showing the pointing stability of the electron beam with and without using the saturable absorber.

magnetic spectrometer along the propagation line of the laser beam, as mentioned earlier. It is evident that using the saturable absorber, although the average total charge is reduced by a factor of 4, the total electron charge production stability is improved by a factor of 5, estimated by dividing the average values of the total electron charge over the 400 shots of the high contrast to low contrast cases.

Furthermore, at the same detection geometry, we examined the shot-to-shot pointing stability of the electron beam by recording the trace of the electron beam imaged on the scintillating screen. A series of typical shot-to-shot images with and without using the saturable absorber are shown in figure 4, where it becomes evident that the use of the saturable absorber improves substantially the pointing stability of the electron beam, and therefore its quality.

4. The gas density profile

The gas jet density profile was characterized using a Nomarski-type interferometer, the operation principle of which is shown in figure 5. In this setup, a linearly polarized CW He–Ne laser beam was initially expanded to a diameter of 40 mm, with the use of a telescope, and sent through the pulsed-jet gas target, covering a cross sectional area larger than the one of the expanded gas (plum area). The laser beam was then guided in a Wollaston-type birefringent prism, thus resulting in two beams at the exit of the prism, slightly separated and with perpendicular polarizations (ordinary and extraordinary waves).

By adjusting the angle of polarization with a polarizer located between the CCD camera and the Wollaston birefringent prism and the recording time window, the interference pattern between the two beams was obtained. The interference pattern shows fringes that are spatially shifted with respect to the background fringes, where the latter correspond to interference from the area outside the gas target. The information about the gas density is encoded in the recorded interference patterns through the optical phase distribution of the gas jet plume area.

The reconstruction (figure 6) of the initial gas density distribution from the interference patterns (figure 6(a)) was performed using a specialized code developed in IPPL. The first step is to apply a two-dimensional fast Fourier transformation (2D FFT) to the interference pattern (figure 6(b)). Then, the frequencies carrying the information for the gas plume

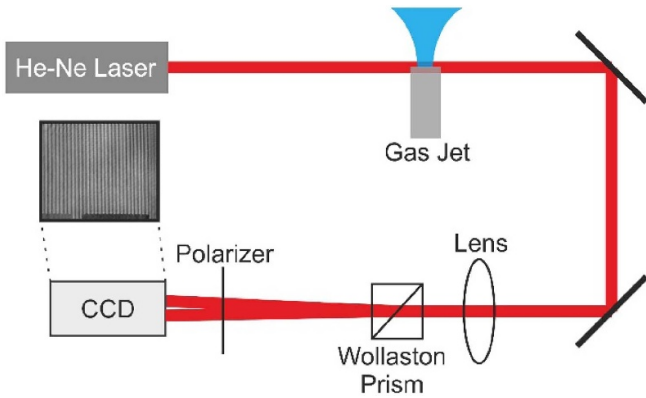


Figure 5. The Nomarski interferometer setup used for the characterization of the gas jet density profile.

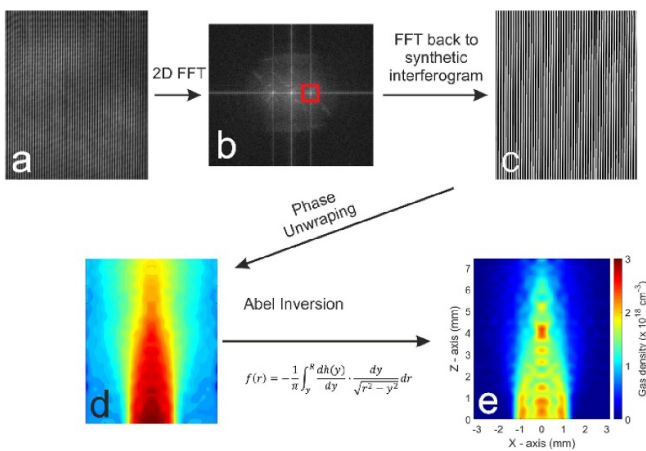


Figure 6. The steps followed by the numerical code for the reconstruction of the 2D gas density profiles from the recorded interferograms. The images are for a gas jet with 3 mm nozzle opening.

density are selected from the 2D FFT pattern. After this, an inverse 2D FFT is applied resulting in a so-called ‘synthetic’ interferogram image (figure 6(c)), i.e. an interferogram having only the frequencies corresponding to the phase shifts. As a next step, a 2D map of the phase shifts is obtained using a phase unwrapping algorithm that exploits the background reference ‘synthetic’ interferogram images (figure 6(d)). Finally, an Abel inversion algorithm is applied to the map of the phase shifts, thus resulting in the 2D gas density distribution (figure 6(e)).

In figure 7 we present the lineouts from the 2D density map of the two nozzles used in the experiments, taken at distance of 1 mm from the jet nozzle. In the case of the 0.8 mm cylindrical nozzle a sharp column of gas was formed reaching a density up to $2 \times 10^{19} \text{ cm}^{-3}$, while the 3 mm conical nozzle generated a trapezoidal gas profile with a maximum density up to $2 \times 10^{18} \text{ cm}^{-3}$. The experimentally measured density profiles for both 0.8 mm and 3 mm nozzles were fitted using a Gaussian and a super-Gaussian function respectively (dashed lines in figure 7). These fitted curves were used as an approximation of the measured density profiles in our PIC models.

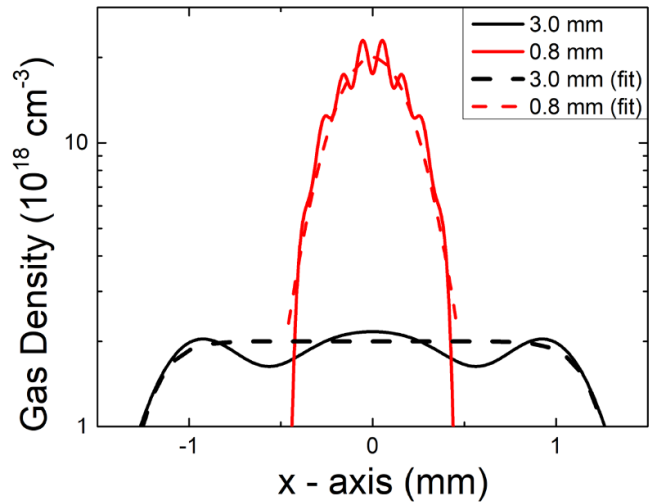


Figure 7. Experimentally measured density lineout profiles for the two gas jet nozzles (solid lines). Dashed lines represent the fitted curves for each profile case that were used as part of the initial parameters in our simulation models.

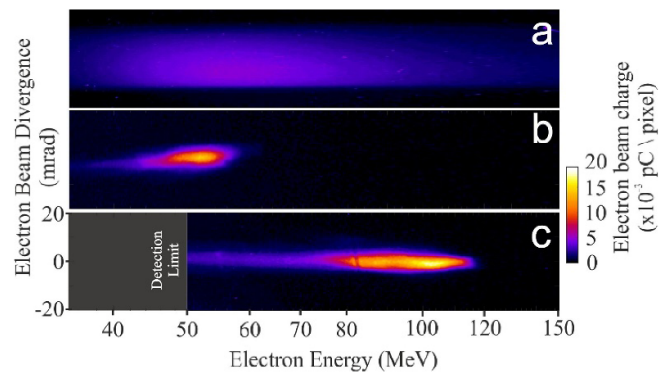


Figure 8. Typical electron spectra using (a) the 0.8 mm cylindrical nozzle without the absorber, (b) the 0.8 mm cylindrical nozzle with the absorber and (c) the 3 mm conical nozzle with absorber.

In figure 8 we present typical electron spectra obtained using the magnetic spectrometer geometry. The electron spectra in figures 8(a) and (b) were both measured using the 0.8 mm cylindrical nozzle but without the use of the absorber for the figure 8(a) case. The effect of the saturable absorber is evident in the spectrum of figure 8(b) where a more intense electron beam is formed around the energy of 50 MeV, as opposed to the large spread in energy and angular distribution for the figure 8(a) case in the absence of the absorber. On the other hand, the 3 mm conical nozzle led to a longer acceleration distance, thus resulting in the generation of electron beams with a maximum energy exceeding 100 MeV and a wider energy spread ($\Delta E/E \cong 34\%$). Using this configuration, the generation of electron beams with maximum energy exceeding 200 MeV has been achieved [13]. The electron beams total charge for both nozzle configurations was determined in the range of hundreds of pC up to a few nC. The above experimental findings are supported by 3D PIC simulation results obtained with the EPOCH code [33].

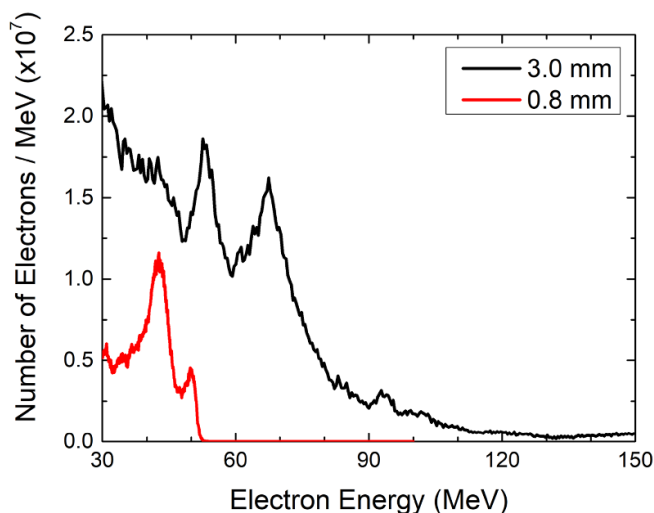


Figure 9. Electron beam spectra simulated by the PIC code EPOCH for both gas jet configurations.

Following the suggestions of [34] for the optimal LWFA modeling and simulation in EPOCH, a 3D PIC model was developed. A computational domain of $120 \times 90 \times 90 \mu\text{m}$ was discretized by $2560 \times 320 \times 320$ cells. A fully ionized helium gas was considered to describe each of the two gas jet density profiles, following the fitted curves of the experimental lineouts (figure 7). The number of particles per cell was 4 with a 3rd order particle shape function. The laser parameters were set according to the reported experimental conditions. Both 0.8 mm and 3 mm nozzle cases were simulated in a moving window configuration for a total simulation time of 3 ps and 12 ps, respectively. Figure 9 shows the simulation results of both models. The qualitative characteristics of the experimental electron spectra are fairly reproduced, showing an extension of the maximum electron energy and a much wider spectrum for the 3 mm conical nozzle density profile, as opposed to the 0.8 mm cylindrical nozzle density profile.

5. Discussion and conclusions

We have presented experimental findings on the optimization of an LWFA relativistic electron source with respect to the laser contrast and the gas density profile. For the laser contrast it was found that a reduction of the ASE pedestal of the laser pulse by two orders of magnitude resulted in an improvement of the electron beam total charge stability, as well as of its pointing stability. For the gas density profile, we showed that using a 0.8 mm in length cylindrical profile resulted in electron beams with a narrow energy spread around an energy of 50 MeV, while using a 3 mm in length conical profile resulted in a wider energy spread exceeding 100 MeV. The data on the gas density profile are supported by PIC simulations.

Data availability statement

The data that support the findings of this study are available upon reasonable request from the authors.

Acknowledgments

We acknowledge support of this work by the project ‘ELI—LASERLAB Europe Synergy, HiPER & IPERION-CH.gr’ (MIS 5002735) which is implemented under the Action ‘Reinforcement of the Research and Innovation Infrastructure’, funded by the Operational Programme ‘Competitiveness, Entrepreneurship and Innovation’ (NSRF 2014-2020) and co-financed by Greece and the European Union (European Regional Development Fund). This work was supported by computational time granted by the Greek Research & Technology Network (GRNET) in the National HPC facility-ARIS—under Project ID pr011027-LaMPIOS. The EPOCH code was developed under the UK EPSRC Grants EP/G054950/1, EP/G056803/1, EP/G055165/1 and EP/M022463/1.

This work has been carried out within the framework of the EUROfusion Consortium, funded by the European Union via the Euratom Research and Training Programme (Grant Agreement No. 101052200—EUROfusion) and the Hellenic National Program of Controlled Thermonuclear Fusion. Views and opinions expressed are however those of the author only and do not necessarily reflect those of the European Union or the European Commission. Neither the European Union nor the European Commission can be held responsible for them. The involved teams have operated within the framework of the Enabling Research Project: ENR-IFE.01.CEA-02 ‘Advancing shock ignition for direct-drive inertial fusion’.

ORCID iDs

I Ftilis  <https://orcid.org/0000-0003-4440-0586>

V Dimitriou  <https://orcid.org/0000-0003-4823-0350>

N A Papadogiannis  <https://orcid.org/0000-0003-0691-2468>

E P Benis  <https://orcid.org/0000-0002-5564-153X>

M Tatarakis  <https://orcid.org/0000-0003-4285-3784>

References

- [1] Tajima T and Dawson J M 1979 Laser electron accelerator *Phys. Rev. Lett.* **43** 267–70
- [2] Tommasini R *et al* 2017 Short pulse, high resolution, backlighters for point projection high-energy radiography at the National Ignition Facility *Phys. Plasmas* **24** 053104
- [3] Mangles S P *et al* 2004 Monoenergetic beams of relativistic electrons from intense laser–plasma interactions *Nature* **431** 535–8
- [4] Geddes C, Toth C, van Tilborg J, Esarey E, Schroeder C, Bruhwiler D, Nieter C, Cary J and Leemans W 2004 High-quality electron beams from a laser wakefield accelerator using plasma-channel guiding *Nature* **431** 538–41
- [5] Faure J, Glinec Y, Pukhov A, Kiselev S, Gordienko S, Lefebvre E, Rousseau J-P, Burgy F and Malka V 2004 A laser–plasma accelerator producing monoenergetic electron beams *Nature* **431** 541–4
- [6] Leemans W P, Nagler B, Gonsalves A J, Tóth C, Nakamura K, Geddes C G, Esarey E, Schroeder C B and Hooker S M 2006 GeV electron beams from a centimetre-scale accelerator *Nat. Phys.* **2** 696–9

- [7] Hafz N A *et al* 2008 Stable generation of GeV-class electron beams from self-guided laser-plasma channels *Nat. Photon.* **2** 571–7
- [8] Wang X *et al* 2013 Quasi-monoenergetic laser-plasma acceleration of electrons to 2 GeV *Nat. Commun.* **4** 1–9
- [9] Kim H T, Pae K H, Cha H J, Kim I J, Yu T J, Sung J H, Lee S K, Jeong T M and Lee J 2013 Enhancement of electron energy to the multi-GeV regime by a dual-stage laser-wakefield accelerator pumped by petawatt laser pulses *Phys. Rev. Lett.* **111** 165002
- [10] Leemans W P *et al* 2014 Multi-GeV electron beams from capillary-discharge-guided subpetawatt laser pulses in the self-trapping regime *Phys. Rev. Lett.* **113** 245002
- [11] Gonsalves A J *et al* 2019 Petawatt laser guiding and electron beam acceleration to 8 GeV in a laser-heated capillary discharge waveguide *Phys. Rev. Lett.* **122** 084801
- [12] Gonsalves A *et al* 2020 Laser-heated capillary discharge plasma waveguides for electron acceleration to 8 GeV *Phys. Plasmas* **27** 053102
- [13] Clark E L *et al* 2021 High intensity laser driven secondary radiation sources using the ZEUS 45 TW laser system at the Institute of Plasma Physics and Lasers of the Hellenic Mediterranean University Research Centre *High Power Laser Sci. Eng.* **9** E53
- [14] Volpe L *et al* 2019 Generation of high energy laser-driven electron and proton sources with the 200 TW system VEGA 2 at the Centro de Laseres Pulsados *High Power Laser Sci. Eng.* **7** E25
- [15] Danson C N *et al* 2019 Petawatt and exawatt class lasers worldwide *High Power Laser Sci. Eng.* **7** E54
- [16] Geddes C G R, Nakamura K, Plateau G R, Toth C, Cormier-Michel E, Esarey E, Schroeder C B, Cary J R and Leemans W P 2008 Plasma-density-gradient injection of low absolute-momentum-spread electron bunches *Phys. Rev. Lett.* **100** 215004
- [17] Mori M *et al* 2009 Generation of stable and low-divergence 10-MeV quasimonoenergetic electron bunch using argon gas jet *Phys. Rev. Accel. Beams* **12** 082801
- [18] Pak A, Marsh K, Martins S, Lu W, Mori W and Joshi C 2010 Injection and trapping of tunnel-ionized electrons into laser-produced wakes *Phys. Rev. Lett.* **104** 025003
- [19] McGuffey C *et al* 2010 Ionization induced trapping in a laser wakefield accelerator *Phys. Rev. Lett.* **104** 025004
- [20] Chen M, Esarey E, Schroeder C, Geddes C and Leemans W 2012 Theory of ionization-induced trapping in laser-plasma accelerators *Phys. Plasmas* **19** 033101
- [21] Mirzaie M *et al* 2015 Demonstration of self-truncated ionization injection for GeV electron beams *Sci. Rep.* **5** 1–9
- [22] Faure J, Rechatin C, Norlin A, Lifschitz A, Glinec Y and Malka V 2006 Controlled injection and acceleration of electrons in plasma wakefields by colliding laser pulses *Nature* **444** 7120
- [23] Faure J, Rechatin C, Lundh O, Ammoura L and Malka V 2010 Injection and acceleration of quasimonoenergetic relativistic electron beams using density gradients at the edges of a plasma channel *Phys. Plasmas* **17** 083107
- [24] Hansson M, Aurand B, Davoine X, Ekerfelt H, Svensson K, Persson A, Wahlström C-G and Lundh O 2015 Down-ramp injection and independently controlled acceleration of electrons in a tailored laser wakefield accelerator *Phys. Rev. Accel. Beams* **18** 071303
- [25] Kim H T *et al* 2017 Stable multi-GeV electron accelerator driven by waveform-controlled PW laser pulses *Sci. Rep.* **7** 10203
- [26] Mangles S P *et al* 2006 Effect of laser contrast ratio on electron beam stability in laser wakefield acceleration experiments *Plasma Phys. Control. Fusion* **48** 12B
- [27] Schumaker W *et al* 2013 Ultrafast electron radiography of magnetic fields in high-intensity laser-solid interactions *Phys. Rev. Lett.* **110** 015003
- [28] Fitisil I *et al* Polymer-gel radiation dosimetry of laser-based relativistic electron sources for biomedical applications *Front. Phys.* under final review
- [29] Andrianaki G, Grigoriadis A, Benis E P and Papadogiannis N A 2020 Pointing characteristics of x-rays generated by relativistic electron acceleration via 45 TW fs laser-He plasma *The 22nd Int. Conf. on Ultrafast Phenomena* (Optical Society of America) (<https://doi.org/10.1364/UP.2020.Tu4A.12>)
- [30] Grigoriadis A, Andrianaki G, Tatarakis M, Benis E P and Papadogiannis N A 2021 Betatron-type laser-plasma x-ray sources generated in multi-electron gas targets *Appl. Phys. Lett.* **118** 131110
- [31] Glinec Y, Faure J, Guemnie-Tafo A, Malka V, Monard H, Larbre J P, de Waele V, Marignier J L and Mostafavi M 2006 Absolute calibration for a broad range single shot electron spectrometer *Rev. Sci. Instrum.* **77** 103301
- [32] Kurz T *et al* 2018 Calibration and cross-laboratory implementation of scintillating screens for electron bunch charge determination *Rev. Sci. Instrum.* **89** 093303
- [33] Arber T D *et al* 2015 Contemporary particle-in-cell approach to laser-plasma modelling *Plasma Phys. Control. Fusion* **57** 113001
- [34] Tazes I, Ong J, Tesileanu O, Tanaka K, Papadogiannis N, Tatarakis M and Dimitriou V 2020 Target normal sheath acceleration and laser wakefield acceleration particle-in-cell simulations performance on CPU & GPU architectures for high-power laser systems *Plasma Phys. Control. Fusion* **62** 094005